

Multimode waveguide-cavity sensor based on fringe visibility detection

Alexander C. Ruege and Ronald M. Reano

*Electroscience Laboratory, Department of Electrical and Computer Engineering,
The Ohio State University, Columbus, OH 43212, USA*
reano@ece.osu.edu

Abstract: Fringe visibility detection of the interaction of two bus spatial eigenmodes with a resonant cavity is investigated for the purpose of achieving a sensor platform with high sensitivity. The power distribution between the bus waveguide eigenmodes is modulated by the interaction with the cavity and is detected via fringe visibility lineshapes produced by twin-fiber interferometry. A test device is fabricated in a polymer-silica material system by a photolithographic process and is characterized by measuring the fringe visibility change as a function of analyte refractive index. Fringe visibility modulation from a straight two-mode waveguide coupled to a single mode ring resonator exposed to an aqueous glucose solution demonstrates a visibility change of 1.57 per weight percent, compared to a transmission change of 0.19 per weight percent for a single mode waveguide critically coupled to a ring with similar intrinsic quality factor. The demonstrated change in fringe visibility is 8.2 times larger.

©2009 Optical Society of America

OCIS codes: (130.3120) Integrated optics devices; (130.6010) Sensors; (230.5750) Resonators (130.5460) Polymer waveguides

References and links

1. A. Ksendzov and Y. Lin, "Integrated optics ring-resonator sensors for protein detection," *Opt. Lett.* **30**, 3344-3346 (2005).
2. C.-Y. Chao, W. Fung, and L. J. Guo, "Polymer microring resonators for biochemical sensing applications," *IEEE J. Sel. Top. Quantum Electron.* **12**, 134-142 (2006).
3. A. Yalcin, K. C. Popat, O. C. Aldridge, T. A. Desai, J. Hryniewicz, N. Chbouki, B. E. Little, O. King, V. Van, S. Chu, D. Gill, M. Anthes-Washburn, M. S. Unlu, and B. B. Goldberg, "Optical Sensing of Biomolecules Using Microring Resonators," *IEEE J. Sel. Top. Quantum Electron.* **12**, 148-155 (2006).
4. C.-Y. Chao and L. J. Guo, "Design and optimization of microring resonators in biochemical sensing applications," *J. Lightwave Technol.* **24**, 1395-1402 (2006).
5. K. De Vos, I. Bartolozzi, E. Schacht, P. Bienstman, and R. Baets, "Silicon-on-Insulator microring resonator for sensitive and label-free biosensing," *Opt. Express* **15**, 7610-7615 (2007).
6. D. X. Xu, A. Densmore, A. Del age, P. Waldron, R. McKinnon, S. Janz, J. Lapointe, G. Lopinski, T. Mischki, E. Post, P. Cheben, and J. H. Schmid, "Folded cavity SOI microring sensors for high sensitivity and real time measurement of biomolecular binding," *Opt. Express* **16**, 15137-15148 (2008).
7. R. W. Boyd and J. E. Heebner, "Sensitive disk resonator photonic biosensor," *Appl. Opt.* **40**, 5742-5747 (2001).
8. E. Krioukov, D. J. W. Klunder, A. Driessen, J. Greve, and C. Otto, "Sensor based on an integrated optical microcavity," *Opt. Lett.* **27**, 512-514 (2002).
9. E. Krioukov, J. Greve, and C. Otto, "Performance of integrated optical microcavities for refractive index and fluorescence sensing," *Sens. Actuators B* **90**, 58-67 (2003).
10. S. Arnold, M. Khoshima, I. Teraoka, S. Holler, and F. Vollmer, "Shift of whispering-gallery modes in microspheres by protein adsorption," *Opt. Lett.* **28**, 272-274 (2003).
11. N. M. Hanumegowda, C. J. Stica, B. C. Patel, I. M. White, and X. Fan, "Refractometric sensors based on microsphere resonators," *Appl. Phys. Lett.* **87**, 201107 (2005).
12. E. Chow, A. Grot, L. W. Mirkarimi, M. Sigalas, and G. Girolami, "Ultracompact biochemical sensor built with two-dimensional photonic crystal microcavity," *Opt. Lett.* **29**, 1093-1095 (2004).
13. N. Skivesen, A. T tu, M. Kristensen, J. Kjems, L. H. Frandsen, and P. I. Borel, "Photonic-crystal waveguide biosensor," *Opt. Express* **15**, 3169-3176 (2007).

14. M. R. Lee and P. M. Fauchet, "Two-dimensional silicon photonic crystal based biosensing platform for protein detection," *Opt. Express* **15**, 4530-4535 (2007).
15. S. Mandal and D. Erickson, "Nanoscale optofluidic sensor arrays," *Opt. Express* **16**, 1623-1631 (2008).
16. I. M. White, H. Oveys, and X. Fan, "Liquid-core optical ring-resonator sensors," *Opt. Lett.* **31**, 1319-1321 (2006).
17. T. Ling and L. J. Guo, "A unique resonance mode observed in a prism-coupled micro-tube resonator sensor with superior index sensitivity," *Opt. Express* **15**, 17424-17432 (2007).
18. V. Zamora, A. Díez, M. V. Andrés, and B. Gimeno, "Refractometric sensor based on whispering-gallery modes of thin capillarie," *Opt. Express* **15**, 12011-12016 (2007).
19. F. Xu, and G. Brambilla, "Demonstration of a refractometric sensor based on optical microfiber coil resonator," *Appl. Phys. Lett.* **92**, 101126 (2008).
20. A. M. Armani, R. P. Kulkarni, S. E. Fraser, R. C. Flagan, and K. J. Vahala, "Label-free, single-molecule detection with optical microcavities," *Science* **317**, 783-787 (2007).
21. S. Fan, "Sharp asymmetric line shapes in side-coupled waveguide-cavity systems," *Appl. Phys. Lett.* **80**, 908-910 (2002).
22. C.-Y. Chao and L. J. Guo, "Biochemical sensors based on polymer microrings with sharp asymmetrical resonance," *Appl. Phys. Lett.* **83**, 1527-1529 (2003).
23. Y. Xiao, V. Gaddam, and L. Yang, "Coupled optical microcavities: an enhanced refractometric sensing configuration," *Opt. Express* **16**, 12538-12543 (2008).
24. M. Sumetsky, "Optimization of optical ring resonator devices for sensing applications," *Opt. Lett.* **32**, 2577-2579 (2007).
25. B. T. Lee and S. Y. Shin, "Mode-order converter in a multimode waveguide," *Opt. Lett.* **28**, 1660-1662 (2003).
26. L. J. Pelz and B. L. Anderson, "Practical use of the spatial coherence function for determining laser transverse mode structure," *Opt. Eng.* **34**, 3323-3328 (1995).
27. K. R. Hiremath, R. Stoffer, and M. Hammer, "Modeling of circular integrated optical microresonators by 2-D frequency domain coupled mode theory," *Opt. Commun.* **257**, 277-297 (2006).
28. A. Hardy and W. Streifer, "Coupled mode theory of parallel waveguides," *J. Lightwave Technol.* **3**, 1135-1146 (1985).
29. A. Yariv, "Universal relations for coupling of optical power between microresonators and dielectric waveguides," *Electron. Lett.* **36**, 321-322 (2000).
30. U. Fano, "Effects of Configuration Interaction on Intensities and Phase Shifts," *Phys. Rev.* **124**, 1866-1878 (1961).
31. K. Okamoto, *Fundamentals of Optical Waveguides* (Academic Press, 2006).
32. I. M. White and X. Fan, "On the performance quantification of resonant refractive index sensors," *Opt. Express* **16**, 1020-1028 (2008).
33. Y. Liu, P. Hering, J., and M. O. Scully, "An Integrated Optical Sensor for Measuring Glucose Concentration," *Appl. Phys. B* **54**, 18-23, (1992).

1. Introduction

Optical resonant cavities have been an integral factor in the development of highly sensitive refractive index sensors in biological and chemical applications. Refractive index biosensing based on rings [1-6], disks [7-9], spheres [10, 11], photonic crystal cavities [12-15], cylindrical capillary cavities [16-18], fiber coils [19], and microtoroids [20] have been investigated. In many designs, the resonant cavity mode is excited by the coupling of light from a single mode waveguide. The output transmission spectrum is a Lorentzian with a lineshape slope that depends on the coupling and quality factor of the resonator. Asymmetrical Fano lineshapes have been demonstrated for cases incorporating partially reflecting elements on the bus waveguide [21, 22] or for multiple coupled resonators [23] and have shown enhanced lineshape slopes. Sharp lineshapes are desirable in a sensor application because they allow the resonance wavelength to be pinpointed to a greater degree of accuracy and give a larger change in intensity at a fixed wavelength for a shift in resonance due to a change in analyte refractive index.

In this paper, fringe visibility detection of the interaction of two bus spatial eigenmodes with a resonant cavity is investigated for the purpose of achieving a sensor platform with high sensitivity. The power distribution between the bus waveguide eigenmodes is modulated by the interaction with the ring cavity and is detected via fringe visibility lineshapes produced by twin-fiber interferometry. Fringe visibility modulation from the two-mode waveguide

coupled to the single mode ring resonator exposed to an analyte sample is then measured as a function of the analyte refractive index.

The sensing mechanism is due to both the response from the ring and the response from the twin fiber interferometer. Experimental results are compared to a single mode resonator, with similar intrinsic quality factor, that is critically coupled to a single mode bus waveguide. Comparison of the multimode waveguide cavity system to a single mode waveguide cavity system allows consistency of the intrinsic quality factor of the resonator in both cases. While the slope of the transmission curve of single mode resonators coupled by single mode waveguides has been shown to be steeper by approximately a factor of 1.2 when not at critical coupling [24], the choice of critical coupling is advantageous in single mode systems when considering other factors such as on/off contrast [4]. It is found that the fringe visibility lineshapes with respect to wavelength for the multimode waveguide-cavity system produce a larger change in visibility, compared to the change in normalized intensity for the single mode waveguide-cavity system, for a given change in analyte refractive index.

The paper is organized as follows. First, multimode bus waveguide interaction with a single mode ring resonator is theoretically analyzed and fringe visibility measurements via twin-fiber interferometry are discussed. Section three discusses optical characterization for the laboratory device. Experimental results are given in section four, followed by concluding remarks in section five.

2. Theory

2.1 Device overview

The device consists of several functional elements, shown in Fig. 1. A single mode input waveguide feeds a mode converter [25], which generates two quasi-TE spatial eigenmodes, $TE_{0,0}$ and $TE_{1,0}$, in the two-mode waveguide with complex amplitudes a_0 and a_1 , respectively. The two modes evanescently couple to the ring waveguide and excite the ring mode. Due to

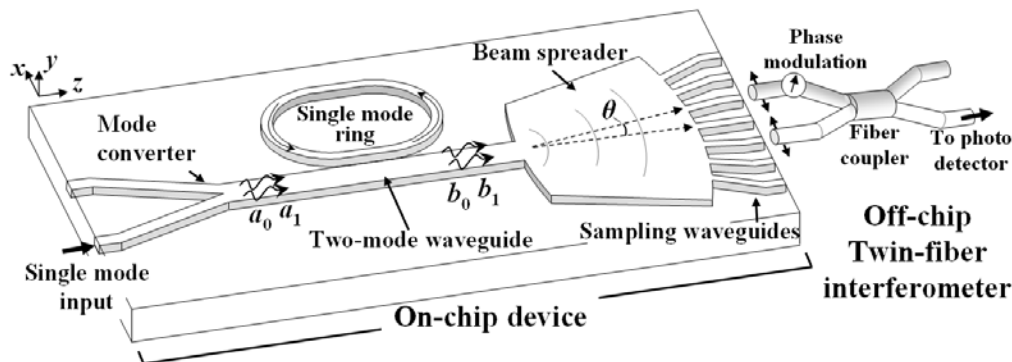


Fig. 1. Schematic of the multimode waveguide-cavity visibility based biosensor.

the different coupling and propagation characteristics of the two eigenmodes, the output amplitudes, denoted b_0 and b_1 for $TE_{0,0}$ and $TE_{1,0}$ respectively, are characterized by different lineshapes with respect to wavelength. At the output of the two-mode waveguide, a beam spreader allows the output field to diffract, enabling wavefront sampling required for twin-fiber interferometry. The off-chip twin-fiber interferometer combines the fields from two symmetric sampling waveguides with a time varying phase delay, producing a fringe intensity pattern at the photodetector. The fringes are characterized by the fringe visibility. The detected fringe visibility lineshapes correspond directly to the modal content of the beam [26].

2.2 Multimode waveguide / single-mode ring coupling

Coupling between $TE_{0,0}$ and $TE_{1,0}$ of the two-mode waveguide and the single eigenmode of the ring waveguide is analyzed by scattering matrix theory, assuming a reciprocal 6-port

network and unidirectional propagation. The electric field profiles of $TE_{0,0}$ and $TE_{1,0}$ are shown in Fig. 2(a). The ports are realized by mode orthogonality and the physical separation of the waveguides [27]. Under these conditions, the full 6x6 scattering matrix is reduced to the following system of equations describing the coupling region shown in Fig. 2(b)

$$\begin{bmatrix} b_0 \\ b_1 \\ b_r \end{bmatrix} = \begin{bmatrix} t_{00} & \kappa_{01} & \kappa_{0r} \\ \kappa_{10} & t_{11} & \kappa_{1r} \\ \kappa_{r0} & \kappa_{r1} & t_{rr} \end{bmatrix} \begin{bmatrix} a_0 \\ a_1 \\ a_r \end{bmatrix}, \quad (1)$$

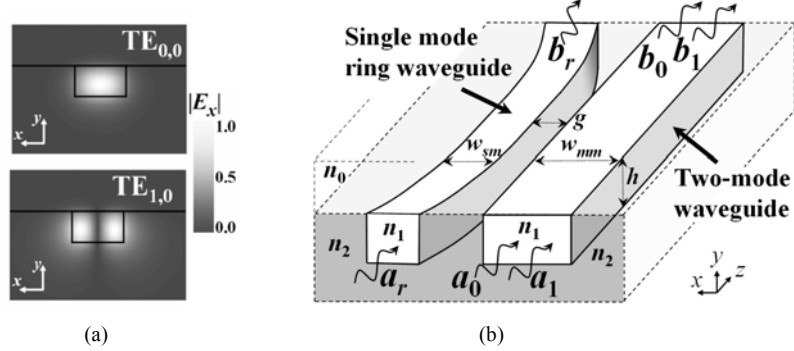


Fig. 2. (a) Electric field profiles of $TE_{0,0}$ and $TE_{1,0}$ of multimode waveguide calculated by beam propagation method. (b) Coupling region of the straight two-mode waveguide and single mode ring waveguide with the following dimensions: waveguide height, h , multimode width, w_{mm} , single mode width, w_{sm} , and gap, g . The refractive indices are n_1 for the core, n_2 for the bottom cladding, and n_0 for the top cladding.

where coupling coefficients are denoted κ_{mn} and transmission coefficients are denoted t_{mn} ($m = 0,1,r$; $n = 0,1,r$). The ring input and output amplitudes are denoted a_r and b_r , respectively. The eigenmode amplitudes are normalized such that their squared magnitudes correspond to the modal power. Power conservation requires that the sum of the squared magnitudes of the elements of each column of the matrix of Eq. (1) must be equal to or less than one.

The coupling between eigenmodes is affected by differences in mode confinement and the phase mismatch. In general, the $TE_{0,0}$ field of a two-mode waveguide is more confined than the field of $TE_{1,0}$. Therefore, less field of $TE_{0,0}$ extends into the ring waveguide compared to that of $TE_{1,0}$. From coupled mode theory, the greater overlap into the coupled waveguide results in greater coupling between the two coupled eigenmodes [28]. For the coupling structure under consideration, the propagation constants of all three eigenmodes are different, resulting in phase mismatch between the eigenmodes. Therefore, the differences in mode confinement have a greater effect on coupling than the phase mismatch. The total power coupled into the ring waveguide from Eq. (1), with $a_r = 0$, results from the interference of the two coupled fields into the ring waveguide as follows:

$$|b_r|^2 = |\kappa_{r0}|^2 |a_0|^2 + |\kappa_{r1}|^2 |a_1|^2 + 2|\kappa_{r0}||\kappa_{r1}||a_0||a_1| \cos(\angle\kappa_{r0} - \angle\kappa_{r1} + \delta_i), \quad (2)$$

where $\delta_i = \angle a_0 - \angle a_1$. Equation (2) demonstrates that the power coupled into the ring waveguide depends on the relative phase difference, δ_i , between the two input eigenmodes at the input of the coupling region. Maximum power coupling into the ring waveguide, for a fixed input power distribution, occurs for $\delta_i = \delta_i^{\max} = \angle\kappa_{r1} - \angle\kappa_{r0} + 2n\pi$, for n integer. Minimum power coupling occurs for $\delta_i = \delta_i^{\min} = \delta_i^{\max} + \pi$.

2.3 Multimode waveguide-cavity interaction

The matrix elements of Eq. (1) are calculated by the effective index method and the finite difference time domain (FDTD) technique in two dimensions (FullWAVE, RSoft, Inc.). Multimode waveguide-cavity outputs are determined by incorporating the ring feedback with

Eq. (1), as done for all-single mode waveguide resonators [29]. The feedback due to the ring waveguide relates a_r and b_r as

$$a_r = b_r t_r \quad (3a)$$

$$t_r \equiv \exp(-L_r \rho/2 - j\beta L_r), \quad (3b)$$

where the length of the ring from the output of the coupling region to the input of the coupling region is L_r , the power attenuation coefficient is ρ and the propagation constant of the ring mode is β . All optical losses including material losses, bending losses, and surface scattering losses are incorporated in ρ . The loss of the ring may be neglected in the coupling region because the ring circumference is much larger than the coupling region length. By combining the feedback of Eq. (3) with the system of Eq. (1), the output mode field amplitudes of the multimode waveguide coupled to the single mode ring are

$$b_0 = t_{00}a_0 + \kappa_{01}a_1 + \kappa_{0r}b_r t_r \quad (4a)$$

$$b_1 = \kappa_{10}a_0 + t_{11}a_1 + \kappa_{1r}b_r t_r, \quad (4b)$$

where the field amplitude inside the ring, b_r , is

$$b_r = (\kappa_{r0}a_0 + \kappa_{r1}a_1)/(1 - t_r t_{rr}). \quad (5)$$

Ring resonances occur when the sum of the phase shift due to the ring outside of the coupling region and the phase shift at the ring-coupling section, $\angle t_{rr}$, is an integer multiple of 2π

$$\angle t_{rr} - \beta L_r = 2\pi n. \quad (6)$$

The output lineshapes of b_0 and b_1 are manifested in several ways and depend on δ_i . Figure 3(a) shows the output modal power distribution for $\delta_i = \delta_i^{\max}$ and input mode power of 0.5 for both eigenmodes. Both output modes exhibit a Lorentzian lineshape at wavelengths 1548.8 nm and 1550.2 nm. At these two wavelengths, the round-trip phase shift in the ring is an integer multiple of 2π . The extinction ratio for the TE_{0,0} mode is 4.1 dB, whereas the extinction ratio for the TE_{1,0} mode is 28.3 dB. The difference in extinction ratios is due to the difference in coupling coefficients. Figure 3(b) shows the output modal power distribution for

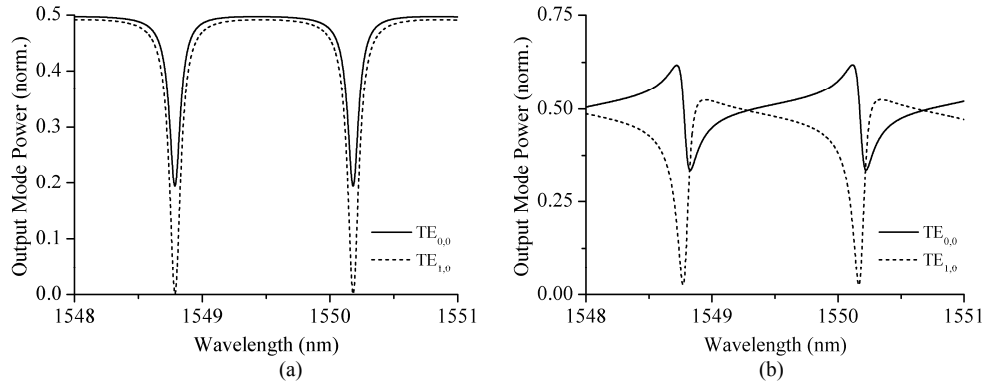


Fig. 3. (a) Output power mode response for $\delta_i = \delta_i^{\max}$ normalized to the total input power ($\rho = 13$ dB/cm). (b) Output power mode response for $\delta_i = \delta_i^{\max} + \pi/2$ normalized to the total input power. The magnitudes and phases of the coefficients obtained at 1.55 μm are $|t_{00}| = 0.988$, $|t_{11}| = 0.914$, $|t_{rr}| = 0.895$, $|\kappa_{01}| \approx |\kappa_{10}| \approx 0.032$, $|\kappa_{0r}| \approx |\kappa_{r0}| \approx 0.145$, and $|\kappa_{1r}| \approx |\kappa_{r1}| \approx 0.400$, $\angle t_{00} = 1.02$, $\angle t_{11} = -0.10$, $\angle t_{rr} = -3.09$, $\angle \kappa_{01} = -0.02$, $\angle \kappa_{10} = -1.85$, $\angle \kappa_{0r} = -1.58$, $\angle \kappa_{r0} = 0.65$, $\angle \kappa_{1r} = 1.09$, and $\angle \kappa_{r1} = -1.12$ for dimensions $h = 1.5$ μm , $w_{mm} = 2.5$ μm , $w_{sm} = 1.4$ μm , $g = 1.0$ μm , and ring radius of 150 μm with a straight coupling section of 10 μm . The refractive indices are $n_1 = 1.57$, $n_2 = 1.44$, and $n_0 = 1.33$. The lengths of the ring waveguide and the two-mode waveguide in the simulation window were both 140 μm .

$\delta_i = \delta_i^{\max} + \pi/2$. The lineshapes are asymmetrical in this case. The interference of $TE_{0,0}$, $TE_{1,0}$ and the ring mode give rise to these Fano lineshapes [30]. The modulation of the power distribution between the bus waveguide eigenmodes is detected via fringe visibility lineshapes produced by twin-fiber interferometry.

2.4 Fringe visibility

Twin-fiber interferometry involves the measurement of visibility obtained via wavefront sampling, where the visibility is a function of modal content [26]. The wavefront is sampled in the far-field at symmetric far-field angles of $\pm\theta$ by sampling waveguides placed at the end of the beam spreader. Two spatial points of the far-field are interfered together by coupling the light from the output of the sampling waveguides into two arms of an optical fiber directional coupler. A time varying phase delay φ in one input arm produces fringes at the photodiode output characterized by visibility, V

$$V = (I_{\max} - I_{\min}) / (I_{\max} + I_{\min}), \quad (7)$$

where I_{\max} is the maximum intensity of the fringes and I_{\min} is the minimum intensity of the fringes over $\varphi = [0, 2\pi]$.

The visibility as a function of θ depends on the output relative phase difference between bus waveguide eigenmodes, δ_o , and the mode power ratio, P_0/P_1 , where $P_0 \equiv |b_0|^2$ and $P_1 \equiv |b_1|^2$. The far-field radiation patterns of the waveguide field at the output of the beam spreader are evaluated by applying the Fourier transform approximation of the Fresnel-Kirchhoff diffraction formula [31]. P_0/P_1 and δ_o are calculated from Eq. (4) for $\delta_i = \delta_i^{\max}$ and equal input mode power distribution corresponding to the lineshapes of Fig. 3(a). As shown in Fig. 4(a), both P_0/P_1 and δ_o change rapidly at the ring resonance wavelength of 1550.18 nm. Therefore the depth and the angular location of the visibility minimum will quickly change at resonance. The resulting visibility is shown in Fig. 4(b) for three different far-field angles of 7.92° , 13.39° and 18.85° . The central peaks in visibility of the three lineshapes correspond to the ring resonance, where P_0/P_1 is very large. These visibility lineshapes demonstrate lineshape slopes that may be exploited in biological sensing.

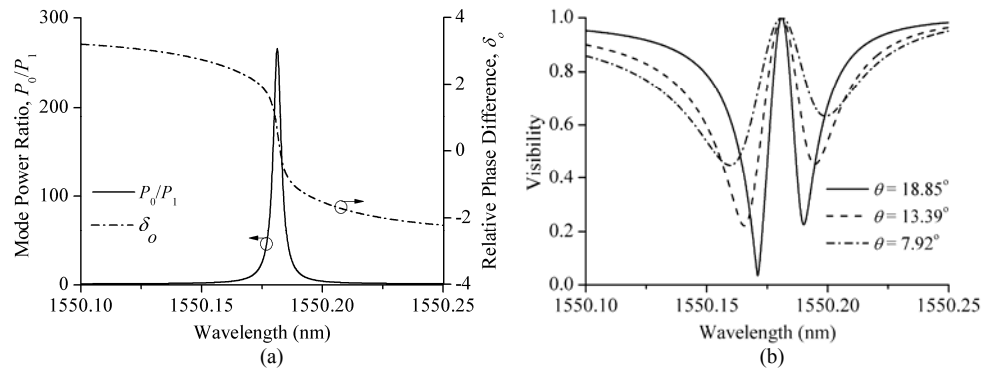


Fig. 4. (a) Output mode power ratio, P_0/P_1 , and output relative phase difference δ_o , for the lineshape of Fig. 3(a) where $\delta_i = \delta_i^{\max}$ and equal input power distribution. (b) Visibility lineshapes calculated from Fig. 3(a) at three far-field angles: 7.92° , 13.39° and 18.85° .

2.5 Refractive index sensing

Resonant-cavity sensors may be based on the resonance wavelength shift caused by a change in effective index of the ring mode, n_{eff} . This change may be due to a change in refractive index of the analyte sample which composes a portion of the ring waveguide structure. The change in resonant wavelength due to a change in analyte refractive index, n_a , depends on the fraction of optical intensity that exists in the analyte, η , as [32]:

$$\frac{\partial \lambda}{\partial n_a} = \eta \frac{\lambda}{n_{eff}}. \quad (8)$$

The resonance shift depends on the waveguide design of the resonator and the location of the analyte sample and is independent of the type of coupling. In two-mode bus waveguide coupling, the output mode amplitude lineshapes, b_0 and b_1 , shift equally in wavelength because they have equal dependence on the ring transmission which is affected by the change in n_a . Thus, the visibility lineshape shifts in wavelength by the same amount as b_0 and b_1 . At a fixed wavelength, the visibility will change due to a change in n_a . The visibility sensitivity to the change in n_a is

$$S = s_V \frac{\partial \lambda}{\partial n_a}, \quad (9)$$

where the visibility lineshape slope with respect to wavelength is denoted s_V . Equation (9) is applicable when the change in wavelength is small so that the visibility lineshape is approximately linear at the bias wavelength. To obtain high sensitivity, s_V should be as large as possible.

The result of Eq. (9) is similar to the intensity variation sensing scheme for all single mode resonator sensors [4]. For an identical ring cavity, the sensitivity in this case depends on s_I , the intensity lineshape slope with respect to wavelength. The shift in resonance wavelength is the same as in the visibility detection scheme. From coupled mode theory, the output intensity, I , of the single mode bus waveguide coupled to a single mode resonator is, assuming lossless coupling [31],

$$I = 1 - \frac{(1-x^2)(1-y^2)}{(1-xy)^2 + 4xy \sin^2(2\pi L n_{eff} / \lambda)}, \quad (10)$$

where x the field transmission through the ring, given by $x = \exp(-L \rho/2)$, y is the bus waveguide field transmission coefficient at the coupling, L is the ring length, and ρ is the power attenuation coefficient. At critical coupling, $x = y$, the maximum s_I is determined from Eq. (10) to be approximately

$$s_I|_{\max} \approx \frac{3\sqrt{3}}{8} \frac{Q_i}{\lambda}, \quad (11)$$

where Q_i is the intrinsic quality factor, given by [6]

$$Q_i = \frac{\pi \sqrt{x} L n_g}{(1-x)\lambda}, \quad (12)$$

where n_g is the group index of the ring mode. The maximum s_I is located at the wavelength corresponding to 0.25 of the maximum transmission.

3. Fabrication and optical characterization

Laboratory test structures were fabricated on a silicon substrate with polystyrene cores and silicon dioxide cladding by a photolithographic process. The dimensions of the ring waveguide and multimode waveguide are nominally the same as discussed in section two. An optical micrograph of the fabricated device is shown in Fig. 5.

Light from a continuous wave tunable infrared laser source is coupled into the single mode input waveguide of the mode converter through a tapered optical fiber. At the end of the beam spreader, sampling waveguides are equally spaced by 0.54° from a far-field angle of -27° to $+27^\circ$. The input fibers of a 50/50 single mode fused fiber coupler are positioned at the output of two of the sampling waveguides. Light exiting from the cleaved output surface

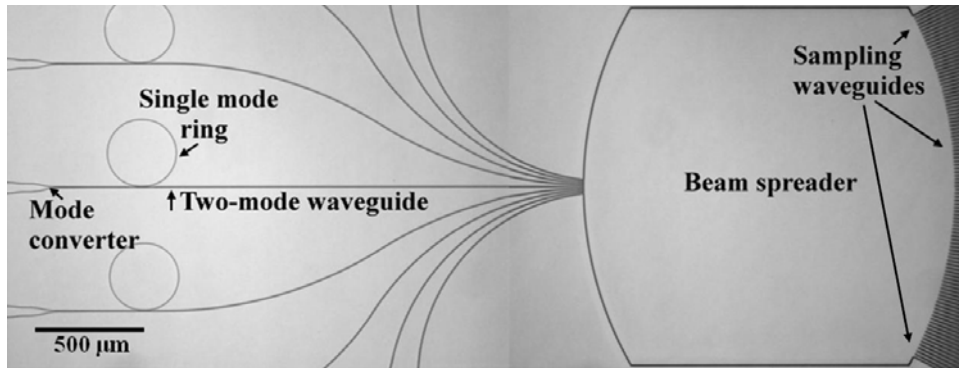


Fig. 5. Optical micrograph of fabricated test device showing mode converter, single mode ring, two-mode waveguide, beam spreader and the sampling waveguide inputs at the end of the beam spreader.

of a sampling waveguide is coupled into one input fiber of the coupler. One fiber is wrapped around a piezoelectric stretcher to produce a time varying phase difference between the two input arms. To match the state of polarization in the two arms, a polarization controller is used in conjunction with the other input fiber. The light in the two fibers is interfered at the coupler, the output of which is directed into a photodetector where the interference fringes are measured with a power meter.

For comparison, on the same chip, the transmission spectrum of a similar single mode ring coupled via a single mode waveguide was characterized, yielding a Q_i of 27,138 with air top-cladding. The same resonator was characterized with water top-cladding, yielding a Q_i of 21,670. The transmission data of both measurements are shown in Fig. 6. For both cases, the x and y parameters were determined by curve fitting Eq. (10) to the measured data.

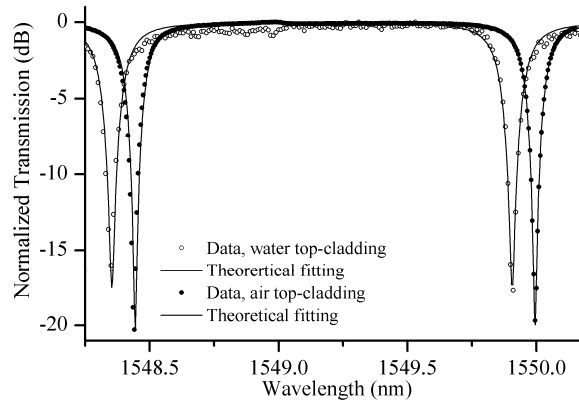


Fig. 6. The transmission spectrum for a single-mode waveguide coupled to a single mode ring. The fitting parameters for air top-cladding are $x = 0.910$ ($\rho = -8.5$ dB/cm), $y = 0.925$. The fitting parameters for water top-cladding are $x = 0.8656$ ($\rho = -13.0$ dB/cm), $y = 0.8953$. The single mode waveguide coupled to the single mode ring was fabricated on the same chip as the two-mode waveguide coupled to a similar single mode ring for the purpose of comparison.

4. Biosensing experiment

Refractive index sensing was performed with varying concentrations of glucose in de-ionized (DI) water. The aqueous glucose solution served as the top cladding of the ring resonator. Different concentrations were detected by measuring the change in fringe visibility at a fixed wavelength.

A 10 μ L drop of DI water was initially placed on the chip using an adjustable volume micropipette. The micropipette was fixed to a three-axis translation stage and positioned over

the ring resonator under test. The drop covered the single mode ring and the full length of the two-mode waveguide from the mode-converter to the beam spreader. Figure 7 shows the location of the drop with respect to the ring resonator and two-mode waveguide. The entire two-mode waveguide was covered so that the propagation of the two eigenmodes was not

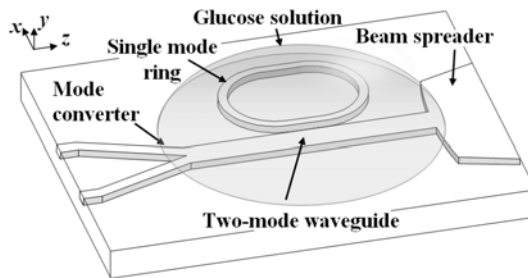


Fig. 7. Location of glucose droplet on the device chip showing complete coverage of the two-mode waveguide.

affected by solution coverage differences between trials. Next, a drop of 1 wt% glucose solution was placed in the same drop by micropipette. By varying the volume of the glucose solution from 1 μL to 10 μL , the concentration covering the ring resonator was varied from 0.091 wt% to 0.5 wt%. For each trial, the previous test liquid was removed from the chip by applying a directed air flow and a new DI water drop was applied to mitigate a change in glucose concentration due to water evaporation. The visibility was measured at a far-field angle of $\theta = \pm 22.6^\circ$ as a function of wavelength for DI water top-cladding and glucose solution top-cladding.

Fringes in intensity at the photodetector were produced by driving the piezoelectric stretcher with a saw-wave voltage. Two cycles of a fringe measurement as a function of time are shown in Fig. 8(a). The low frequency sinusoidal signal is the fringe created by the drive voltage. The higher frequency fringes at times 0.2 s and 0.4 s were created when the drive voltage returned to the beginning of a new cycle. The maximum and minimum power is recorded from the measurement of the fringes and the visibility is calculated using Eq. (7) during the data acquisition. Figure 8(b) shows the maximum and minimum intensities measured as the wavelength was swept for water top-cladding.

After the 10 μL DI water was first dispensed onto the chip, the visibility was measured as a function of wavelength. The visibility measured for water top-cladding and two glucose concentrations is shown in Fig. 9(a). Theoretical fitting curves calculated using the theory

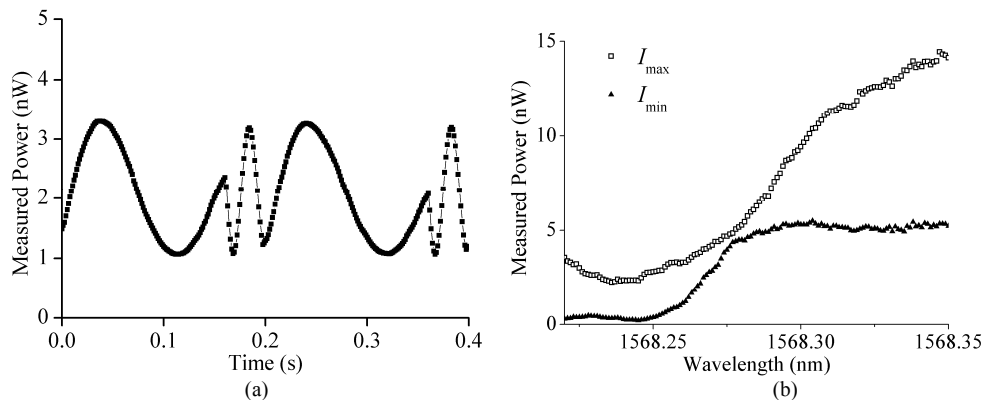


Fig. 8. (a) Fringes in measured power for a saw-wave drive. The visibility is 0.51. (b) The maximum and minimum powers measured for water top-cladding.

presented in section two are also shown. The visibility measured with DI water corresponds to the measured I_{max} and I_{min} of Fig. 8(b). Immediately after the visibility was characterized

for DI water top-cladding, the wavelength was biased on the steep slope of the visibility lineshape (near 1568.265 nm). As the glucose solution was added, the visibility at this wavelength was measured as a function of time, as shown for two trials in Fig. 9(b). The solution was added at time 0 s. Transient behavior, likely due to diffusion, was observed immediately after the glucose solution was added. The visibility was found to quickly increase to a maximum value then slowly decrease to a constant value. This data indicates that the refractive index sensed by the ring resonator was highest immediately after the

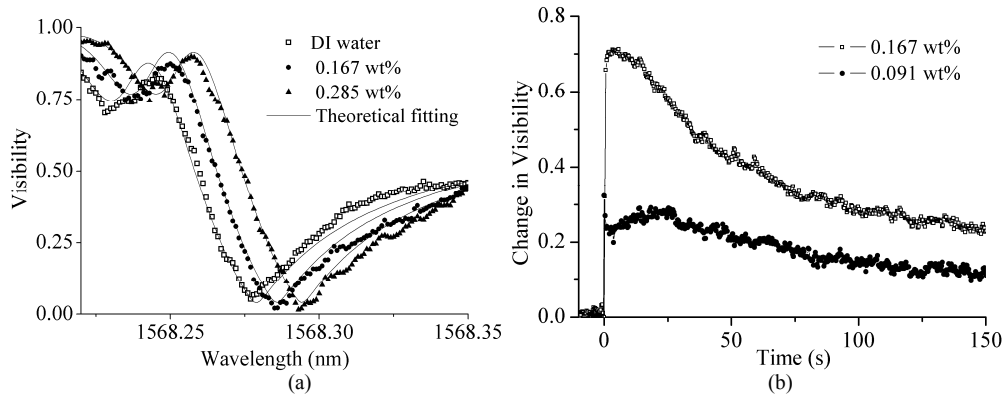


Fig. 9. (a) Visibility experimentally measured at $\theta = \pm 22.6^\circ$ for DI water, 0.167 wt% and 0.285 wt% glucose in DI water with theoretical fittings. (b) Change in visibility as the glucose solution was added to change the concentration of the drop on the chip surface.

glucose solution was added and slowly decreased thereafter to steady state. Visibility as a function of wavelength was measured after steady state was reached. The visibility lineshapes measured with water top-cladding and with glucose solution top-cladding are observed to have the same shape. The shift in wavelength due to the effective index change of the ring waveguide is therefore more significant than coupling changes or propagation changes in the two-mode waveguide due to a change in top-cladding index over the two-mode waveguide.

The largest change in visibility between the DI water visibility data and glucose solution visibility data was recorded for four trials for six different glucose concentrations. The average visibility change for the six concentrations and best-fit line is shown in Fig. 10. The measurements demonstrate a visibility change of 1.57 per wt% glucose in water. Assuming

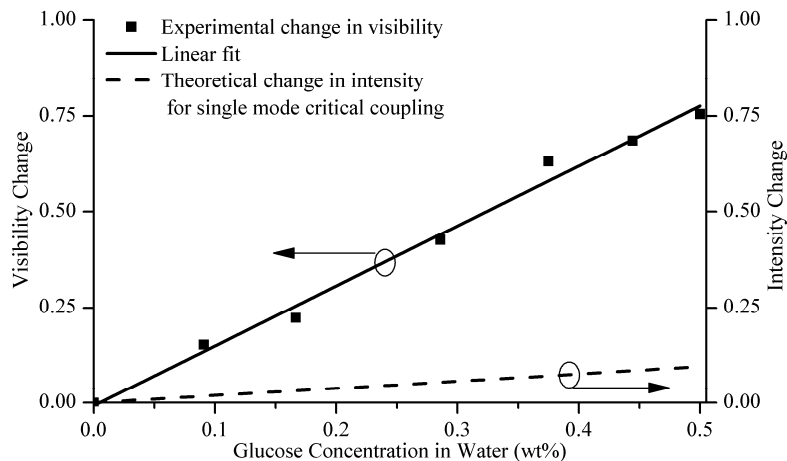


Fig. 10. Change in detected visibility measured experimentally as a function of glucose concentration in water, with theoretical change in normalized transmission intensity of a single mode coupled resonator at critical coupling.

1.4×10^{-3} RIU/wt% for glucose concentration in water [33], the visibility will change by 1,120 per RIU.

From Eq. (11), the maximum slope in intensity for the all single mode device with a Q_i of 21,670 at critical coupling is 9 nm^{-1} . Coupled mode theory predicts a change of 0.19 per wt%, as shown in Fig. 10. The intensity will therefore change by 136 per RIU. The change in visibility is 8.2 times larger. To obtain an intensity change of 1.57 per wt%, a resonator with a Q_i of 177,000 is required for the all single mode system at critical coupling.

The performance of the device is achieved with an increase in complexity in the system. Complexity arises from the need to generate and control two eigenmodes, and the need to detect via twin-fiber interferometry. The design process must account for multiple distinct spatial modes in the ring waveguide-bus waveguide coupling region. In the current prototype, the interferometry is accomplished off-chip thereby requiring simultaneous alignment of two external fibers. Driving electronics for the time varying phase delay are also needed for the twin-fiber interferometer. The interferometer may be placed on-chip in future designs by employing electro-optic control, thus eliminating the drawbacks associated with the off-chip interferometer.

5. Conclusion

In this paper, fringe visibility detection of the interaction of two bus spatial eigenmodes with a resonant cavity is investigated for the purpose of achieving a sensor platform with high sensitivity. A theoretical analysis is conducted and an experimental demonstration is performed in a biosensor application. The output mode power distribution is found to be a strong function of the relative phase difference between modes. Individual mode responses may exhibit Lorentzian or asymmetrical lineshapes due to the multimode interference at the coupling region. By using the twin-fiber interferometry technique, the output visibility is measured as the optical wavelength is swept through a ring resonance. A test device with a polystyrene core and silicon dioxide cladding is fabricated and its performance as a biosensor is characterized. The measurements of different aqueous glucose concentrations, presented to the device as the ring resonator top-cladding, demonstrate a visibility change of 1.57 per wt% (1,220 per RIU). Coupled mode theory predicts a change of 0.19 per wt% (136 per RIU) at critical coupling for an all-single mode device with an intrinsic quality factor of 21,670. The measured change in visibility is 8.2 times larger than the theoretical change in intensity for a critically coupled all-single mode resonator.